Progress In Electromagnetics Research C, Vol. 117, 73–87, 2021

Compact Differential Tri-Band Bandpass Filter with Multiple Zeros Using Sext-Mode Stepped-Impedance Square Ring Loaded Resonator

Ziyue Guo[1], Litian Wang[4], Rong Guo[1], Yang Xiong[5], Ming He[1, 2, 3, *], Lu Ji[1], and Xu Zhang[1]

Abstract—In this paper, a second-order tri-band balanced bandpass filter (BPF) with multiple transmission zeros (TZs) and compact size is presented. The structure consists of novel stepped impedance square ring loaded resonators (SI-SRLRs), which can excite six resonance modes. For design of SI-SRLR, we analysed the odd-mode equivalent circuit and obtained the electrical lengths from the design graph. Meanwhile, the wider frequency distances between differential modes (DMs) and common modes (CMs) are realized by selecting the proper admittance ratio of SI-SRLR. Then for design of BPF, six TZs are introduced by source-load coupling, which lead to band-to-band isolation of 23 dB. Additional T-shaped stubs and open stubs are loaded on the symmetric plane of SI-SRLR, which result in high CM suppressions of 43 dB, 25 dB, and 37 dB at three DM centre frequencies. Finally, a tri-band differential BPF operating at 1.46 GHz, 4.45 GHz, and 5.48 GHz is fabricated and measured. The measured 3-dB fractional bandwidths of three passbands are 6.8%, 7.4%, and 5.6%. A wide DM and CM stopband suppression of 20 dB is achieved to 14.6 GHz ($10f_0$). The measurements verify well the proposed structure and the design method.

1. INTRODUCTION

With the rapid development of modern communication techniques, balanced bandpass filters (BPFs) have attracted substantial attention due to their high immunity to electromagnetic (EM) interference, crosstalk, and environmental noise. Many scholars have done a lot of research on balanced filters. Moreover, as multi-band operations are widely used in wireless RF systems [1–8], balanced multi-band BPFs are urgently required nowadays

For dual-band balanced BPFs, stub-loaded resonators (SLRs) [9, 10], stepped impedance resonators [10–12], and coupled lines [13] are most commonly used to realize dual-band performances. To improve the common-mode (CM) suppression, additional terminating microstrip stubs [9, 14, 15, 16] and lumped elements [10, 11, 15] are loaded on the symmetric plane of a differential filter. By tuning the electrical parameters of loaded elements, the CM suppression performance can be optimized. New material is also applied to design dual-band balanced filters. In [17], a fourth-order dual-band high temperature superconducting balanced filter based on square ring loaded resonators (SRLRs) is developed, which implements the low insertion loss.

To the best of our knowledge, few works can achieve tri-band BPFs with differential characteristics. In [18], a compact balanced tri-band BPF based on SLRs is firstly proposed and analysed. Four rectangular defected ground structures are employed to increase the coupling between the I/O port and the SLR. However, the BPF suffers from poor band-to-band isolation of 15.8 dB. Thereafter, a

Received 24 September 2021, Accepted 1 December 2021, Scheduled 20 December 2021

* Corresponding author: Ming He (heming@nankai.edu.cn).

[1] College of Electronic Information and Optical Engineering, Nankai University, Tianjin 300350, China. [2] China Tianjin Key Laboratory of Optoelectronic Sensor and Sensing Network Technology, Tianjin 300350, China. [3] Engineering Research Centre of Thin Film Photo-electronics Technology, Ministry of Education, China. [4] College of Electrical and Electronic Engineering, Tianjin University of Technology, Tianjin 300384, China. [5] Southwest China Institute of Electronic Technology, Chengdu 610036, China.

tri-band balanced filter with improved band-to-band isolation of 48 dB is proposed by using multi-stub resonators [19], while the ideal selectivity of each side band is hard to accomplish with only three transmission zeros (TZs). In [20], three pairs of uniform impedance resonators are coupled to realize the tri-band performance. The quasi-elliptical bandpass responses of the filter enhance the side band selectivity, and slotline coupled-feed structure enhances the CM suppression. However, the stopband to $2.8f$ need to be further improved. In summary, there is still space to be further improved for tri-band differential operations.

In this paper, a balanced tri-band BPF with six TZs, compact size, and high level of passband isolation has been designed based on novel stepped-impedance square ring loaded resonators (SI-SRLRs). The analysis of the SI-SRLR and how to determine the electrical size of SI-SRLR are given in Section 2. The design of the tri-band differential filter is given in Section 3, including the source-load coupling, bandwidth, and common mode performance. In Section 4, the simulated and measured results of the filter verify the proposed method. Compared with above-mentioned tri-band designs, there exist two different designing techniques:

(1) For differential mode (DM) operation, we analyse and calculate the design graph of varied frequency ratios versus electric lengths. Then according to centre frequency specifications, the corresponding electrical lengths of proposed SI-SRLR can be obtained.

(2) By exploring the varied resonance frequency versus loading location of the cross-shaped stub resonator, it is found that all resonance frequencies keep constant. This effective property can be used to shorten the length of nearby source-load (S-L) coupled line, therefore avoiding its resonance mode affects high-frequency passband and still maintaining sufficient coupling strength to produce six TZs.

2. ANALYSIS OF PROPOSED SEXT-MODE SI-SRLR

In Section 2, we mainly design the electrical parameters of the resonator. The design strategy is as follows. Under the proposed SI-SRLR, firstly use odd-mode analysis method to calculate and plot the design graph. Then according to the desired centre frequencies, the corresponding electrical parameters can be obtained from the design graph. Secondly, choose the appropriate admittance ratio to keep the CMs away from the DMs. In summary, the electrical size of the SI-SRLR is basically determined.

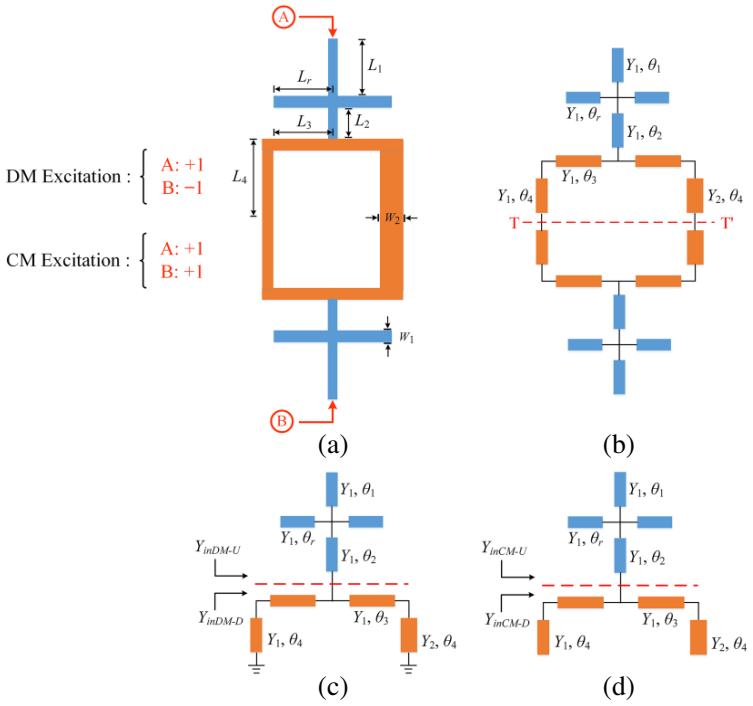

Figure 1. Proposed sext-mode SI-SRLR and equivalent TLM. (a) Sext-mode SI-SRLR. (b) Ideal TLM. (c) DM equivalent circuit. (d) CM equivalent circuit.

2.1. Equivalent Circuit of SI-SRLR

Figure 1(a) shows the geometry of the proposed sext-mode SI-SRLR. It consists of one stepped-impedance square ring and a pair of horizontal loaded cross-shaped stubs. L_1, L_2, L_3, L_4, L_r and W_1, W_2 stand for physical lengths and widths of corresponding microstrip lines. The equivalent transmission line model (TLM) of the proposed SI-SRLR is depicted in Figure 1(b). Y_1, Y_2 and θ_1, θ_2, θ_3, θ_4, and θ_r denote the characteristic admittances and electrical lengths of specific transmission lines.

The configuration is symmetrical to dashed plane T-T'; therefore, the classical odd-mode and even-mode analysis method can be employed to interpret the resonant features. Under odd-mode excitation (with respective to DM excitation), the symmetrical plane T-T' acts as a perfect electrical wall, and its equivalent circuit is shown in Figure 1(c). Y_{inDM-U} and Y_{inDM-D} respectively stand for the input admittance of upward and downward of the red dashed line. Under even-mode excitation (with respective to CM excitation), the symmetrical plane T-T' acts as the magnetic wall. Its equivalent circuit is shown in Figure 1(d). Y_{inCM-U} and Y_{inCM-D} represent the input admittances of upward and downward of the red dashed line. In following parts, DM and CM resonant characteristics will be investigated and designed separately based on odd-mode/even-mode analysis method and equivalent TLM simulations.

2.2. Analysis of DM Resonances

To simplify analysis, let $\theta_r = \theta_3$. Based on presented DM equivalent circuit and microwave transmission line theory, the DM resonant frequencies can be calculated by setting Im $(Y_{inDM-U} + Y_{inDM-D}) = 0$, as follows:

$$(\tan\theta_1 + \tan\theta_2 + 2\tan\theta_3) \times \tan(\theta_3 + \theta_4) \times (k\tan\theta_3 + \tan\theta_4) + [1 - \tan\theta_2 \times (\tan\theta_1 + 2\tan\theta_3)] \times [\tan(\theta_3 + \theta_4) \times (\tan\theta_3 \times \tan\theta_4 - k) - k\tan\theta_3 - \tan\theta_4] = 0 \quad (1)$$

where

$$Y_{inDM-U} = jY_1 \frac{\tan\theta_1 + \tan\theta_2 + 2\tan\theta_3}{1 - \tan\theta_2 \times (\tan\theta_1 + 2\tan\theta_3)} \quad (2)$$

$$Y_{inDM-D} = jY_1 \frac{\tan(\theta_3 + \theta_4) \times (\tan\theta_3 \times \tan\theta_4 - k) - k\tan\theta_3 - \tan\theta_4}{\tan(\theta_3 + \theta_4) \times (k\tan\theta_3 + \tan\theta_4)} \quad (3)$$

The admittance ratio k of SI-SRLR is defined as $k = Y_2/Y_1$. It can be seen from Eq. (1) that both the varied electrical lengths and admittance ratio k influence DM resonance frequencies. By solving Eq. (1), three DM frequencies are obtained and denoted as f_{d1}, f_{d2}, and f_{d3}. Then the resonance performances will be investigated in detail.

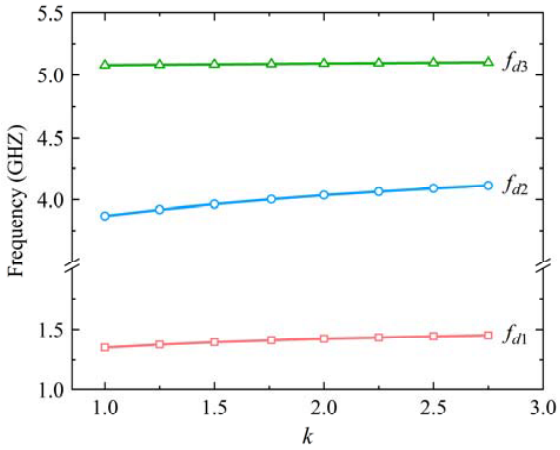

Figure 2. Variations of DM frequency versus different admittance ratio k (under the specific parameters of $\theta_1 = 35°$, $\theta_2 = 25°$, $\theta_3 = \theta_r = 25°$ and $\theta_4 = 25°$).

Firstly, the DM frequency responses versus varied admittance ratio k are calculated and drawn in Figure 2 by numerical calculation software MATLAB, under the specific electrical parameters of $\theta_1 = 35°$, $\theta_2 = 25°$, $\theta_3 = \theta_r = 25°$ and $\theta_4 = 25°$. It is obvious that three DMs almost keep constant when the k varies. Therefore, for simplicity, k is set to 1.5 preliminarily in next analyzations.

Secondly, to explain the influence of main electric parameters on resonance frequencies, we investigate and depict the variations of three DMs versus θ_1, θ_2, θ_3, θ_4, and θ_r in Figure 3. Figures 3(a) and (b) show that θ_1, θ_2, and θ_3 all influence f_{d1}. From Figure 3(c), we find that θ_4 influences f_{d2} and f_{d3}, while f_{d1} is hardly affected. Moreover, θ_r only manages f_{d3} in Figure 3(d). Thereby, different from the harmonic passbands, three DM passbands can be controlled independently as follows: Simultaneously change the θ_1, θ_2, and θ_3 to approach accurate f_{d1}. Afterwards, by choosing proper θ_4, the ideal f_{d2} is designed without affecting f_{d1}. Finally, tune θ_r to realize the required f_{d3}, and f_{d1} and f_{d2} remain unchanged. From these relationships between electrical lengths and resonance frequencies, the characteristics of SI-SRLR can be further analysed.

We next investigate how to determine the accurate electrical parameters based on the ideal centre frequencies. To relieve the complicity of DM analyzations, the fundamental frequency should be determined primarily. Figure 3 shows that f_{d1} is influenced by θ_r, θ_1, θ_2, and θ_3, except θ_4. Thereby in order to find out the specific relationship among these electrical lengths, we choose f_{d1} as the fundamental frequency f_0.

After that, according to the proposed SI-SRLR, the fundamental electrical length corresponding to fundamental frequency f_0 is obtained as $\theta = \theta_1 + \theta_2 + 2\theta_r + 2\theta_3$. The ideal f_{d1} is 1.5 GHz,

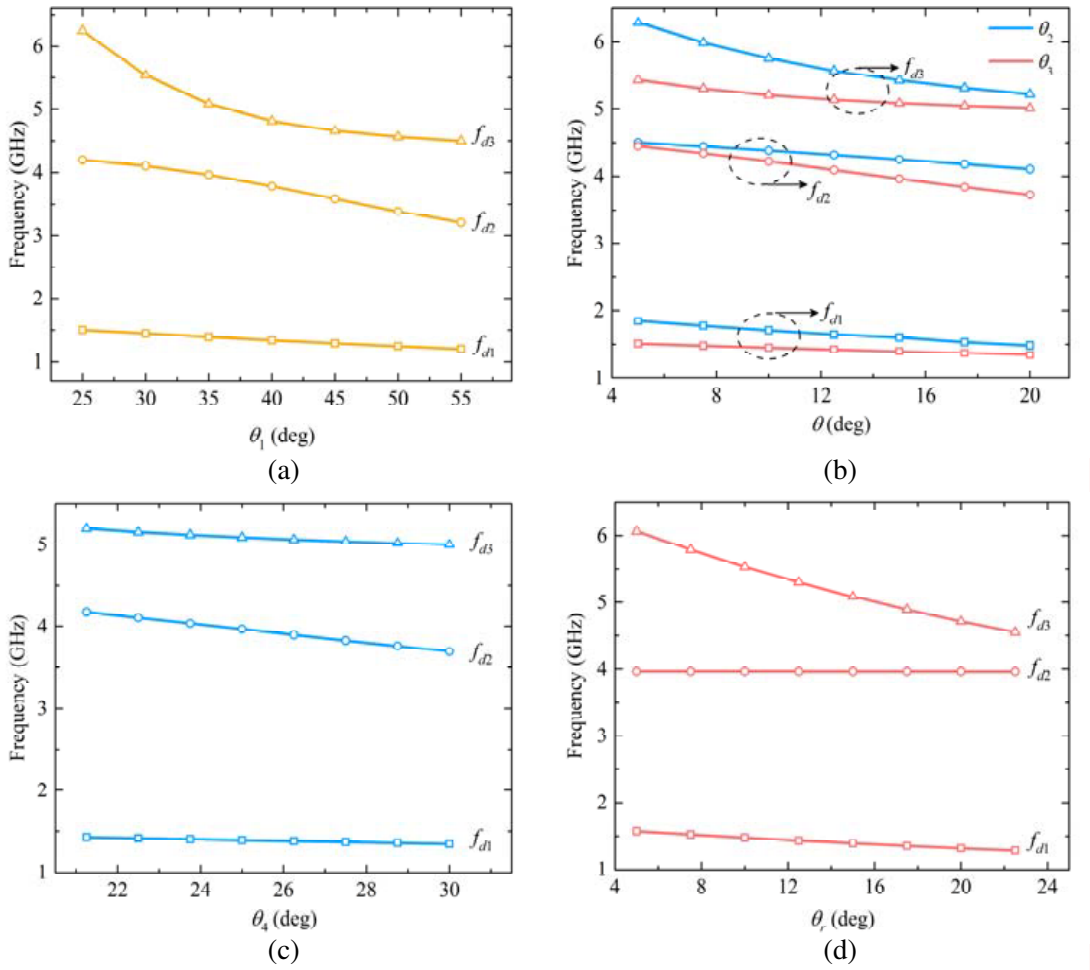

Figure 3. DM frequencies of SI-SRLR with varied (a) θ_1, (b) θ_2 and θ_3, (c) θ_4, (d) θ_r (under the specific parameter of $k = 1.5$).

so $f_0 = f_{d1} = 1.5\,\text{GHz}$. Then based on TLM simulations, the fundamental electrical length θ_0 is approximately satisfied as:

$$\theta_0 = \theta_1 + \theta_2 + 2\theta_r + 2\theta_3 = 105^\circ \tag{4}$$

Herein with varied θ_1 and θ_2, θ_3 can be calculated from Eq. (4). For normalizing DM frequencies, we set $r_i = f_{di}/f$ $(i = 1, 2, 3)$. Thereby the relationship of electrical lengths and resonance frequencies is written as:

$$\theta_i' = \theta_i \times f_{di}/f_0 = \theta_i \times r_i \tag{5}$$

In order to simplify the solved electrical parameters, set θ_4 to 25°. Finally, based on Eq. (1), Eq. (4), and Eq. (5), the variations of DM frequency ratios (f_{d3}/f_{d1}, f_{d2}/f_{d1}) versus θ_1, θ_2, and θ_3 with $\theta_4 = 25^\circ$ and $k = 1.5$ are derived and drawn in Figure 4 by utilizing calculator MATLAB. According to the design graph and Eq. (4), the resonant frequencies specifications can be satisfied by properly choosing θ_1, θ_2, and θ_3. For example, the desired DM resonant frequencies of SI-SRLR are specified at 1.55, 4.3, and 5.65 GHz, respectively. Thus two frequency ratios are extracted as: $f_{d2}/f_{d1} = 4.3/1.55 = 2.77$, $f_{d3}/f_{d1} = 5.65/1.55 = 3.65$. From Figure 4, the parameters of $\theta_1 = 35^\circ$, $\theta_2 = 22.5^\circ$ are indicated with the black pot, and the corresponding θ_3 and θ_r can be calculated as 11.875° from Eq. (4).

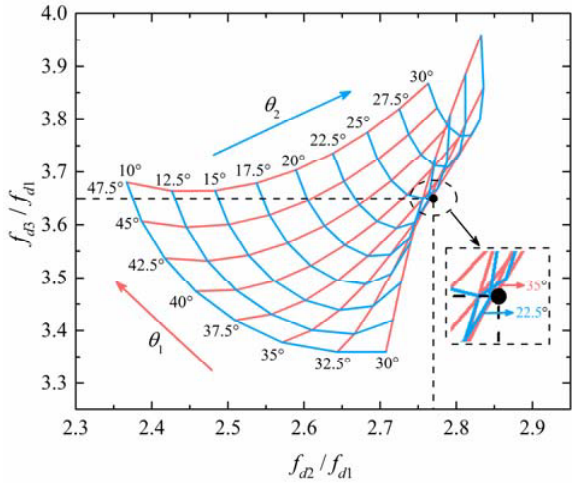

Figure 4. Variations of DM frequency ratios (f_{d3}/f_{d1}, f_{d2}/f_{d1}) versus θ_1, θ_2 and θ_3 under the specific parameters of $k = 1.5$ and $\theta_4 = 25^\circ$.

2.3. Analysis of CM Resonances

Similarly, the CM resonant frequencies are calculated by setting Im $(Y_{inCM-U} + Y_{inCM-D}) = 0$, as follows:

$$\begin{aligned}&(\tan\theta_1 + \tan\theta_2 + 2\tan\theta_3) \times (1 - k\tan\theta_3 \times \tan\theta_4) + [1 - \tan\theta_2 \times (\tan\theta_1 + 2\tan\theta_3)] \\ &\times [\tan(\theta_3 + \theta_4) \times (1 - k\tan\theta_3 \times \tan\theta_4) + \tan\theta_3 + k\tan\theta_4] = 0\end{aligned} \tag{6}$$

where

$$Y_{inCM-U} = jY_1 \frac{\tan\theta_1 + \tan\theta_2 + 2\tan\theta_3}{1 - \tan\theta_2 \times (\tan\theta_1 + 2\tan\theta_3)} \tag{7}$$

$$Y_{inCM-D} = jY_1 \frac{\tan(\theta_3 + \theta_4) \times (1 - k\tan\theta_3 \times \tan\theta_4) + \tan\theta_3 + k\tan\theta_4}{1 - k\tan\theta_3 \times \tan\theta_4} \tag{8}$$

By solving Eq. (6), three CMs are obtained and denoted as f_{c1}, f_{c2}, and f_{c3}, respectively. Based on preliminary selected electrical parameters of $\theta_1 = 35^\circ$, $\theta_2 = 22.5^\circ$, $\theta_3 = \theta_r = 12^\circ$, $\theta_4 = 25^\circ$, and $k = 1.5$, the comparison between the numerical calculation results from MATALB and simulated resonance results from ADS of SI-SRLR is plotted in Figure 5. The numerical calculation results agree well with the simulation ones. Moreover, we find CM f_{c3} is closer than DM f_{d3}.

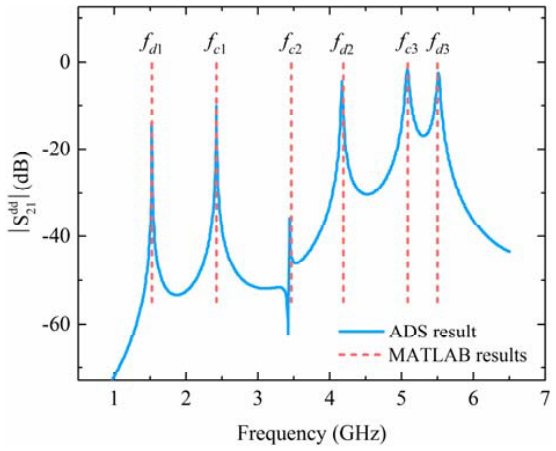

Figure 5. Calculation results and simulation results of SI-SRLR with weak coupling (under the specific parameters of $\theta_1 = 35°$, $\theta_2 = 22.5°$, $\theta_3 = \theta_r = 12°$, $\theta_4 = 25°$ and $k = 1.5$).

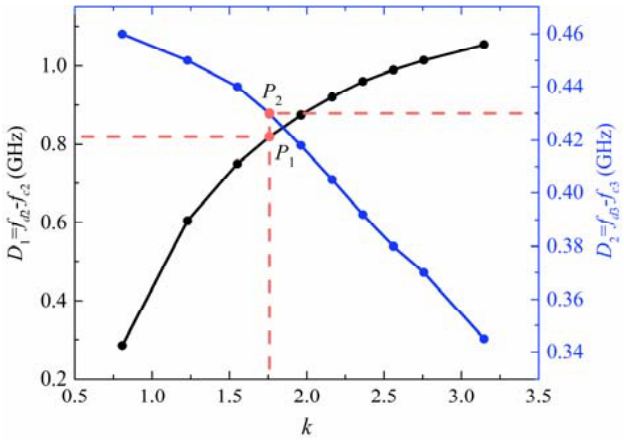

Figure 6. Variations of distance D_1 and D_2 with different admittance ratio k (under the specific parameters of $\theta_1 = 35°$, $\theta_2 = 22.5°$, $\theta_3 = \theta_r = 12°$ and $\theta_4 = 25°$).

Therefore, in order to prevent the CMs from affecting DM passbands, CMs should be shifted far away from DMs while DMs are kept constant. From Eq. (6), both the electrical lengths and admittance ratio k influence CM resonance frequencies. In addition, k does not affect DMs from Figure 2. Thus, by properly choosing the admittance ratio k, CM can be kept away from DM without affecting DM since f_{d3} and f_{c3} are closer, and the preliminary simulation shows that f_{c2} changes greatly under different k. We select f_{c2} and f_{c3} for research. Define $D_1 = |f_{d2}f_{c2}|$, $D_2 = |f_{d3}f_{c3}|$. Then the variations of D_1 and D_2 versus admittance ratio k are simulated by ADS and depicted in Figure 6. Figure 6 shows that when k increases, D_1 increases greatly while D_2 decreases slightly. When $k = 1.76$, the two frequency separations get superior results, respectively. The corresponding distances of D_1 and D_2 are calculated as 0.815 GHz (|4.19–3.375|) and 0.43 GHz (|5.55 − 5.12|).

3. DESIGN OF BALANCED TRI-BAND FILTER

In this section, based on aforementioned analyzations of SI-SRLR, tri-band differential BPF will be designed in detail. The design process is summarized as follows. Firstly, properly select the initial electrical lengths and admittance ratio according to the desired centre frequencies. Secondly, in order to improve band-to-band isolation level and sideband selectivity, we introduce and analyse the S-L coupled lines. Thirdly, investigate the relationship between the fractional bandwidths (FBW) and the coupling strength to meet the desired passbands bandwidths. Fourthly, for enhancing CM suppression, multiple additional stubs are loaded at the symmetrical plane of the differential filter [6–8, 15]. Finally, by using full wave electromagnetic (EM) simulator HFSS 2018, the physical dimensions are optimized.

3.1. Determination of Electrical Parameters

To satisfy the desired centre frequencies of SI-SRLR, the initial electrical lengths are derived from the design graph of Figure 4. The detailed electrical parameter values are as below: $\theta_1 = 35°$, $\theta_2 = 22.5°$, $\theta_3 = \theta_r = 12°$, and $\theta_4 = 25°$. Plus, the admittance ratio k is chosen as 1.76 from Figure 6 to obtain further gaps between DMs and CMs.

The two-order balanced tri-band BPF is designed with centre frequencies of 1.5 GHz, 4.4 GHz, and 5.6 GHz, and 3-dB FBWs of 6.9%, 6.1%, and 8.8%. The overall configuration of the balanced filter is shown in Figure 7. The stub l_1 is folded for compact size. The balanced tri-band filter will be designed and simulated based on full-wave EM simulator. Herein, the substrate is selected as Rogers4003C with a thickness of 0.508 mm, loss tangent of 0.0029, and relative dielectric constant of 3.55.

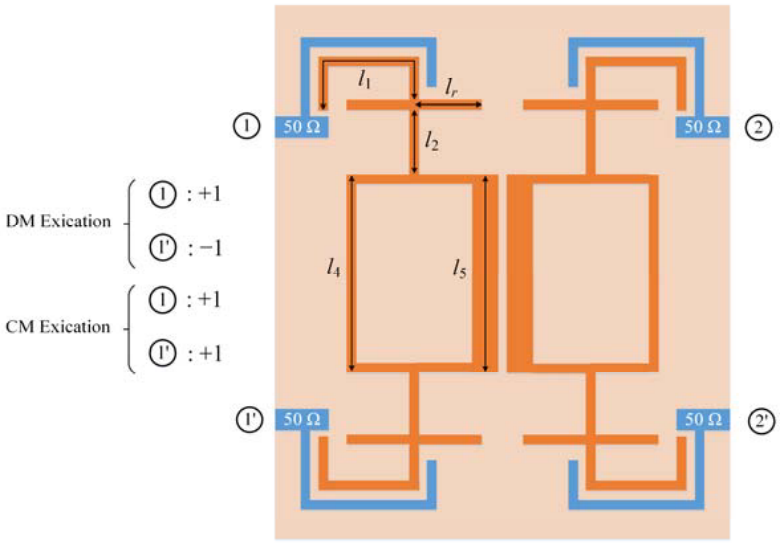

Figure 7. Initial configuration of balanced tri-band BPF.

3.2. Design of S-L Coupled Lines

The frequency response of initial differential filter in Figure 7 is shown as blue dashed line in Figure 8. It is observed that the passband selectivity should be further improved, and the coupling characteristics of the third passband need to be properly adjusted. Introducing an additional transmission path from the source port to the load port is a commonly used method to generate transmission zeros. Therefore, in order to achieve superior passband selectivity, a pair of S-L coupled lines will be added and analysed in the geometry.

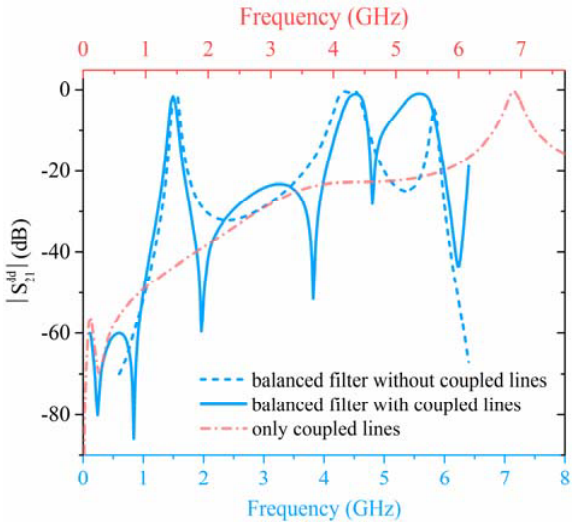

Figure 8. DM simulation results of balanced BPF with or without coupled lines.

To select the appropriate location of S-L coupled lines, current density distribution of three DMs should be analysed first. Figure 9 shows that current density mainly concentrates on the whole SI-SRLR without the l_r segments at f_{d1}. Current density mainly focuses on l_1, l_2, l_4, and l_5 segments at f_{d2}. For f_{d3}, current density concentrates on the whole cross-shaped stubs. We find the segment l_r only

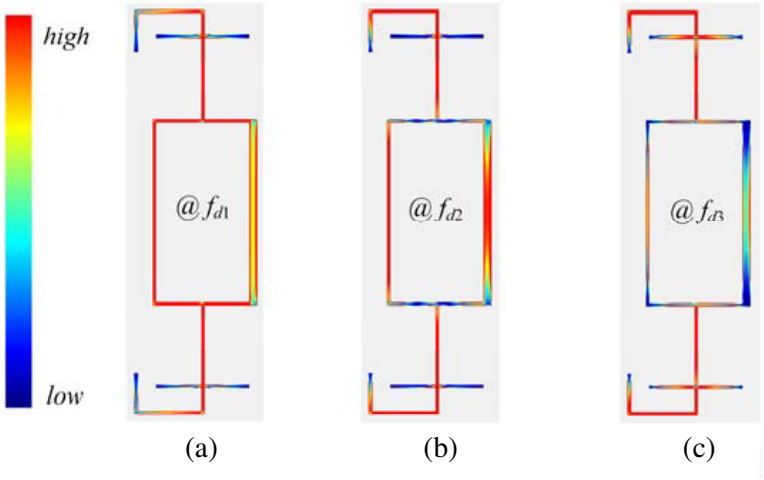

Figure 9. Simulated current density distribution of SI-SRLR at three DM resonance frequencies, (a) f_{d1}, (b) f_{d2}, (c) f_{d3}.

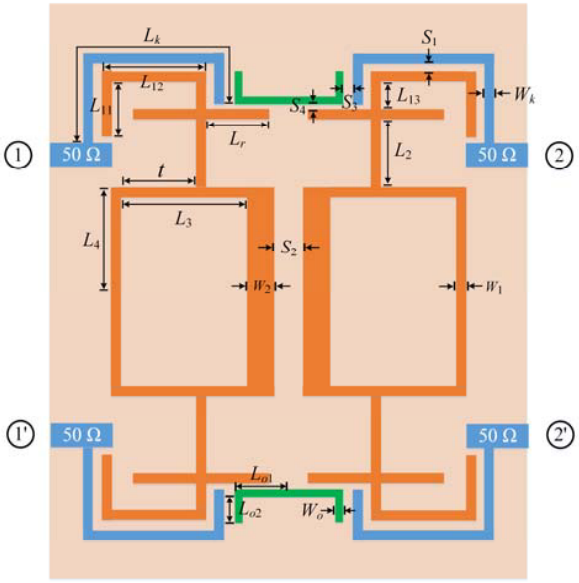

Figure 10. Modified configuration of balanced tri-band BPF.

resonates at f_{d3}. Therefore, a pair of S-L coupled green lines with length of L_o and width of W_o is added close to the blue feed lines and the l_r segment in Figure 10. This selection has the following two purposes. Firstly by changing the length of S-L coupled line, different numbers of TZs can be achieved. Meanwhile, by adjusting the gap between S-L coupled line and the l_r segment, desired coupling level of the third passband can be obtained.

It is noticed that the S-L coupled line also introduces an unwanted mode, which is shown in Figure 8. To relieve its influence on the third DM passband, the over-length coupled line should be avoided. The coupled line is composed of segments l_{o1} and l_{o2} in Figure 10. Based on preliminary simulations, we find that only a longer l_{o2} can obtain sufficient coupling strength to produce multiple TZs. So we choose a shorter l_{o1} to shorten the coupled line without affecting l_{o2}. Fortunately, the loading location of cross-shaped stub has minor influence on three DMs. Therefore by shifting the left and right cross-shaped stubs closer, the shortened l_{o1} can be obtained.

The detailed interpretation about the loading location of cross-shaped stub hardly affects DM

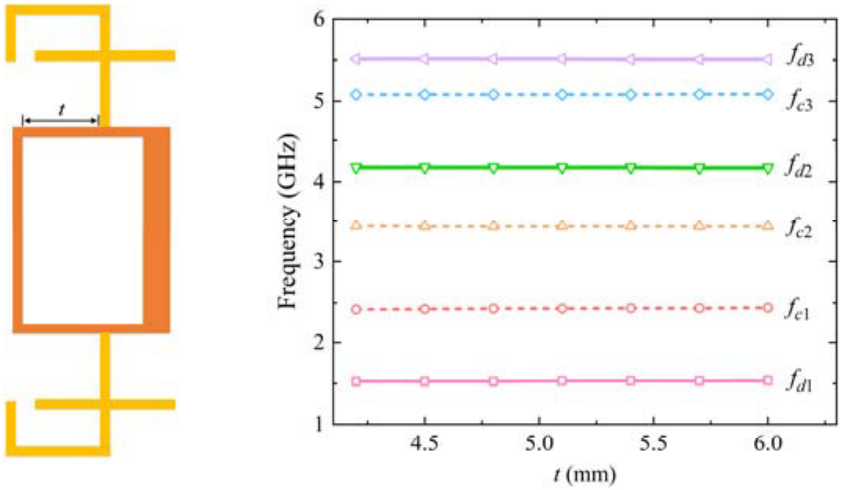

Figure 11. Analysis of the loading location t of cross-shaped stub. (a) Geometry of loaded cross-shaped stub, (b) resonance frequency characteristics with varied t (under the specific $\theta_1 = 35°$, $\theta_2 = 22.5°$, $\theta_r = 12°$, $\theta_4 = 25°$, $k = 1.76$).

response which is organized as follows: Define the location of a cross-shaped stub resonator on a square ring as t, which is shown in Figure 11(a). The variations of six resonance frequencies versus t are depicted in Figure 11(b). It is obvious that both DMs and CMs are constant with varied t. Therefore, the left and right cross-shaped stubs can be moved closer to shorten S-L coupled lines.

The final length of S-L coupled lines is chosen as $1/2\lambda$ wavelength at 7 GHz. Modified geometry is shown in Figure 10. The corresponding DM response is plotted as the blue solid line in Figure 8. Compared with the DM response without S-L coupled lines, six TZs are generated at both sides of each passband, which significantly improve the band-to-band isolation. The optimized parameters of tri-band filter are $\theta_1 = 34.39°$, $\theta_2 = 18.49°$, $\theta_3 = 18.35°$, $\theta_4 = 24.3°$, $\theta_5 = 12.2°$, $\theta_r = 14.99°$, $\theta_{o1} = 13.41°$ and $\theta_{o2} = 5.32°$ at 1.5 GHz, $Y_1 = 0.0107$ S, $Y_o = 0.01008$ S and $k = 1.76$.

3.3. Design of Coupling Structure

For meeting desired passband bandwidths, the coupling structure needs to be designed properly. In this part we will investigate the variation of the bandwidth versus the coupling distances among the resonator, feed line, and S-L coupled line.

Figure 12 provides the simulated FBW curves of three DM passbands versus the gaps S_1, S_2, and S_4. S_1 is the gap between the feed line and the SI-SRLR. S_2 is the gap between the two square ring resonators. S_3 is the gap between the S-L coupled line and the feed line. S_4 is the gap between the S-L coupled line and the cross-shaped stub resonator. It is seen from Figures 12(a) and (b) that both the gaps S_1 and S_2 influence FBW_1, while only gap S_2 affects FBW_2. S_4 shown in Figure 12(c) mainly has influence on FBW_3. Therefore, the three desired bandwidths can be satisfied as follows: Firstly, properly tune the gaps S_1 and S_2 to approach the ideal FBW_1 and FBW_2. Then the wanted FBW_3 can be acquired by tuning the gap S_4 without affecting FBW_1 and FBW_2. Based on the desired FBWs of 6.9%, 6.1% and 8.8%, the final tuned coupling gaps are $S_1 = S_2 = S_3 = 0.1$ mm, $S_4 = 0.11$ mm.

3.4. Loaded Stubs for CM Suppression

From above discussion, the DM design methodology is demonstrated in detail. The corresponding CM transmission response of modified differential filter in Figure 10 is plotted as the dashed line in Figure 14. It is seen that the CM suppressions at three DM centre frequencies are about 41 dB, 14 dB, and 33 dB, and an unwanted CM resonance peak between the first two passbands is excited. Therefore, the CM suppression performance of the balanced filter should be further improved.

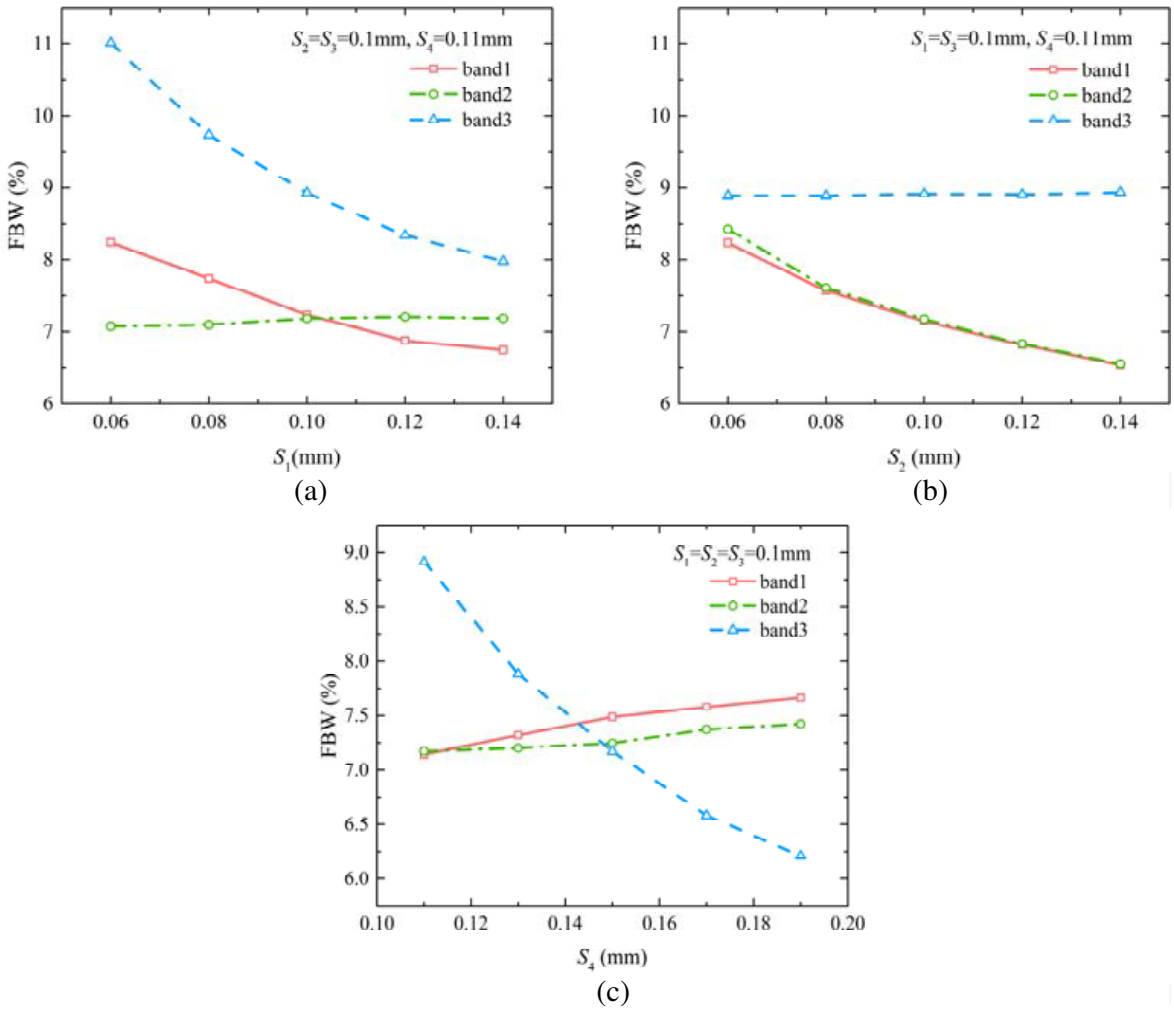

Figure 12. Varied FBW of three DM passbands with different coupling gaps. (a) S_1, (b) S_2, (c) S_4 (under the specific $\theta_1 = 34.39°$, $\theta_2 = 18.49°$, $\theta_3 = 18.35°$, $\theta_4 = 24.3°$, $\theta_5 = 12.2°$, $\theta_r = 14.99°$, $\theta_{o1} = 13.41°$ and $\theta_{o2} = 5.32°$, $k = 1.76$).

For the schematic of the balanced BPF in Figure 13, the symmetrical plane T-T' acts as the perfect electrical wall under DM excitation. Under CM excitation, the symmetrical plane T-T' acts as the magnetic wall. Therefore, by loading additional stubs at the symmetric plane, the CM resonances can be separated, and the CM responses can be further suppressed. Because the symmetry plane is short-circuited under DM excitation, loading additional stubs on this symmetry plane does not affect the DM topology and responses [6–8, 15]. As shown in Figure 13, a microstrip line is added on the symmetric plane to connect the l_4 and l_5 segments of square ring resonator. A pair of T-shaped stub and open stub is loaded on this line. In addition, an open stub is loaded at the symmetric plane of the right ring resonator. By tuning the lengths and locations of T-shaped stubs and open stubs, two CM TZs can be generated near the last two DM centre frequencies to improve in-band CM rejection.

The modified CM transmission characteristics are depicted as the solid line in Figure 14. Figure 14 shows that the optimized CM suppression at three DM centre frequencies is up to 43 dB, 25 dB, and 37 dB. Two CM TZs are generated in last two DM passbands, which significantly enhance the in-band CM suppression. Other four CM TZs are generated among three passbands over a wider frequency band. The CM resonance peak at 2.4 GHz is suppressed from 2 dB to 19 dB.

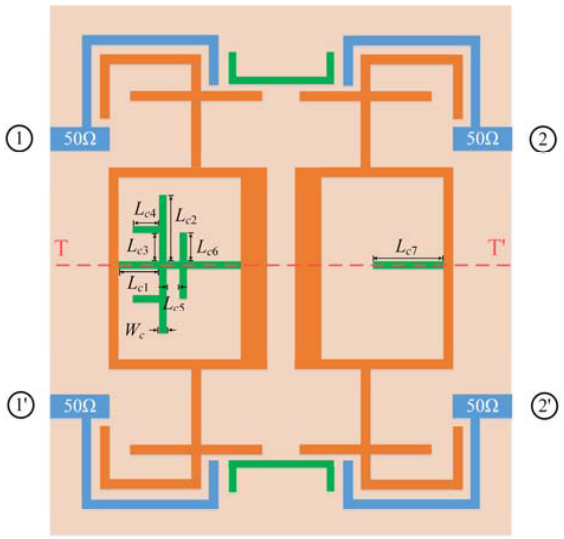

Figure 13. Layout of balanced tri-band BPF with additional stubs loaded at symmetrical plane.

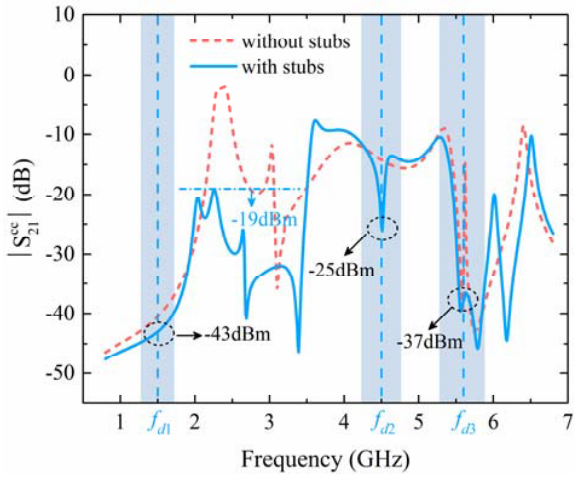

Figure 14. CM simulation results of balanced tri-band BPF with or without additional stubs loaded at symmetrical plane.

4. EXPERIMENTAL RESULT AND DISCUSSION

To verify above analyzations, a sext-mode balanced tri-band BPF is fabricated and measured. After final full-wave EM simulations and optimizations, the geometrical dimensions are selected as follows (units: mm): $w_1 = 0.3$, $w_2 = 1$, $w_k = 0.3$, $w_o = 0.25$, $w_c = 0.525$, $L_{11} = 3.41$, $L_{12} = 6.52$, $L_{13} = 2.1$, $L_2 = 6.5$, $L_3 = 10.44$, $L_4 = 8.5$, $t = 6$, $L_{o1} = 4.69$, $L_{o2} = 1.86$, $L_{c1} = 3.4$, $L_{c2} = 5.975$, $L_{c3} = 2.8$, $L_{c4} = 2.585$, $L_{c5} = 1.05$, $L_{c6} = 2.07$, $L_{c7} = 6.5$, $S_1 = 0.1$, $S_2 = 0.1$, $S_3 = 0.1$, $S_4 = 0.11$. A photograph of fabricated balanced tri-band BPF is shown in Figure 15. The tri-band balanced filter occupies the area of $22.98 \times 35.4\,\text{mm}^2$ (excluding feed lines), which corresponds to $0.179\lambda_g \times 0.276\lambda_g$, where λ_g is the guided wavelength at centre frequency of the first DM passband. The fabricated filter is measured by a four-port Agilent vector network analyser N5247A.

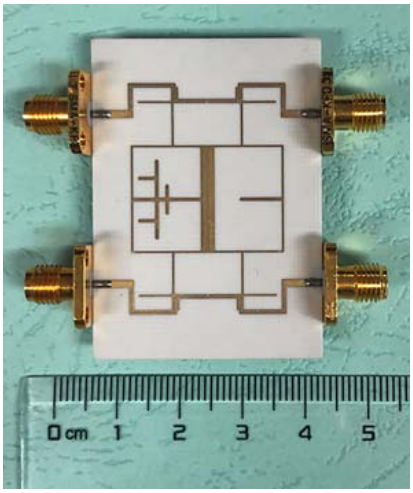

Figure 15. Photograph of fabricated balanced tri-band BPF.

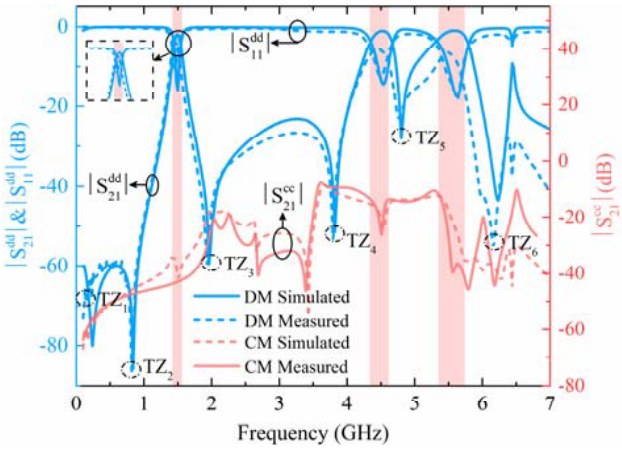

Figure 16. Simulated and measured results of fabricated balanced tri-band BPF.

Figure 16 plots the comparison of measurement and simulated results. For the DM responses, the simulated centre frequencies of three passbands are 1.49 GHz, 4.5 GHz, and 5.53 GHz, with 3-dB FBWs of 7.23%, 7.33%, and 8.9%. The simulated minimal insertion losses of three passbands are 1.98 dB, 1.1 dB, and 0.96 dB, and the return losses are respectively > 16.5 dB, > 156 dB, and > 17.8 dB. Meanwhile, six DM TZs are generated by the upper and lower sides of each passband to improve the selectivity of passbands. For CM response, the simulated CM suppressions at DM centre frequencies are 43 dB, 25 dB, and 37 dB. Six CM TZs are generated within simulated frequency range, which further restrain the transmission of CM response.

For the DM responses, the measured first, second, and third DM passbands of 1.41–1.51 GHz, 4.28–4.61 GHz, and 5.33–5.64 GHz are respectively centred at 1.46 GHz, 4.45 GHz, and 5.48 GHz, with 3-dB FBWs of 6.8%, 7.4%, and 5.6%. The measured minimal insertion losses of three passbands are 3.49 dB, 5.74 dB, and 6.57 dB, and the return losses are > 10.8 dB, > 12.5 dB, and > 18.3 dB, respectively. Six DM TZs are introduced to show good agreements with simulated ones. For CM response, the measured CM suppressions at the DM centre frequencies are 43 dB, 25 dB, and 33 dB, which show a good CM suppression within DM passbands. It is worth noting that there is a gap between measured and simulated insertion losses for the second and third passbands. Based on our analysis, the dissimilarities mainly result from the fabricated tolerance and radiation loss. From EM simulations, we find that a variation

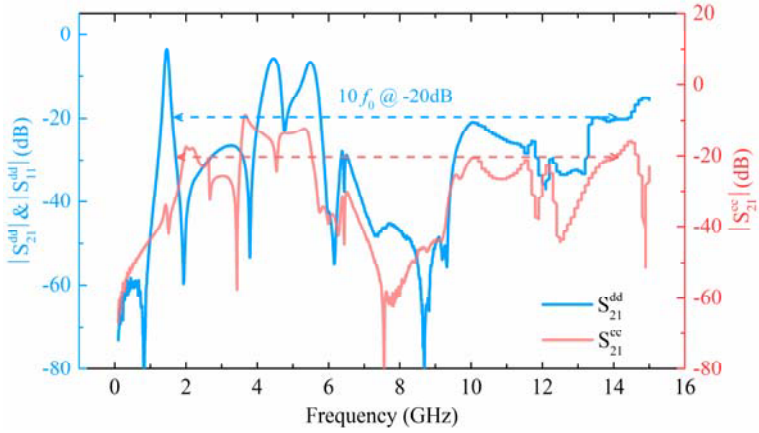

Figure 17. Measured DM and CM response of balanced tri-band BPF in wide frequency range.

Table 1. Comparison of some previous dual-band/tri-band differential/balanced filters.

Ref.	Centre Frequency (GHz)	Insertion loss (dB)	Number of Zeros	Band-to-Band Isolation (dB/GHz)	DM stopband	In-Band CM attenuation (dB)	Circuit size ($\lambda_g \times \lambda_g$)
[16]	0.9/2.49	2.67/4.65	3	40	35 dB@5.6f_0	30/40	0.67 × 0.32
[18]	2.5/3.5/5.8	0.8/2.3/2/4	3	15.8	17.5 dB@5.2f_0	32/31/32	0.25 × 0.21
[19]	1.23/2.39/3.5	1.09/2.15/1.33	3	48.2	20 dB@3.7f_0	25/21/28	0.58 × 0.19
[20]	2.4/3.51/5.2	2.43/3.5/3.6	6	17.5	15 dB@2.8f_0	41/42/41	0.25 × 0.25
[21]	1.9/3.35/5.8	0.94/1.21/1.93	5	17	15 dB@3.7f_0	54/27/32	0.19 × 0.23
[22]	2.45/3.5/4.45	1.44/1.68/2.16	3	7.2	11.8 dB@2.5f_0	46/39/35	0.68 × 0.29
[23]	2.44/5.25	2.4/2.82	0	N/A	55 dB@2.8f_0	55/51	0.84 × 0.76
[24]	9.23/14.05	2.9/2.7	N/A	38.8	38 dB@1.8f_0	48/40	2.7 × 1.27
This work	1.46/4.45/5.48	3.49/5.74/6.57	6	26	20 dB@10f_0	34/25/33	0.18 × 0.28

in coupling gap of 80 microns induces 2 dB insertion loss varieties. Therefore, the fabricated tolerance may be a main cause. Additionally, a small shielding box is set up during simulating process, which is not connected in measurement. Thus the radiation loss may be another important reason, which is far more obvious at higher frequencies.

To further investigate the out of band performance of fabricated tri-band BPF, we measure and depict the DM and CM responses within 15 GHz frequency range in Figure 17. The measured DM and CM stopband suppression is greater than 20 dB to 14.6 GHz ($10f_0$), which achieves an extremely wide stopband feature. The comparison of other reported balanced tri-band/dual-band BPFs is shown in Table 1. It can be seen that the proposed filter outperforms the others in terms of the compact size, number of TZs, band-to-band isolation, and wide stopband suppression.

5. CONCLUSION

In this paper, a two-order balanced tri-band BPF based on novel SI-SRLRs and S-L coupled lines is presented. The proposed tri-band BPF has more degrees of freedom in controlling the DM response with admittance ratio and S-L coupling. Also, its CM suppression has been optimized by loading different stubs on SI-SRLR. The simulated and measured results verify the proposed method well. With the features of multiple TZs, wider DM and CM stopband, desired CM suppression, compact size, and high band-to-band isolation, the balanced tri-band BPF is attractive in applications of balanced multiband wireless systems.

ACKNOWLEDGMENT

The development work has been supported in part by the National Natural Science Foundation of China (Grant No. 61973173), the 111 Project with grant No. B16027 the Engineering Research Centre (Ministry of Education) of Thin Film Photo-electronics Technology, the Key Laboratory of Photoelectronic Thin Film Devices and Technology of Tianjin, the International Cooperation Base for New PV Technology and the Southwest China Institute of Electronic Technology.

REFERENCES

1. Zhou, K., C. X. Zhou, and W. Wu, "Resonance characteristics of substrate-integrated rectangular cavity and their applications to dual-band and wide-stopband bandpass filters design," *IEEE Transactions on Microwave Theory and Techniques*, Vol. 65, No. 5, 1511–1524, 2017.
2. Rahman, M.-U., D.-S. Ko, and J.-D. Park, "A compact triband bandpass filter utilizing double mode resonator with 6 transmission zeros," *Microwave and Optical Technology Letters*, Vol. 60, No. 7, 1767–1771, 2018.
3. Ghaderi, A., A. Golestanifar, and F. Shama, "Design of a compact microstrip tunable dual-band bandpass filter," *AEU — International Journal of Electronics and Communications*, Vol. 82, 391–396, 2017.
4. Ma, M. M., Z. X. Tang, X. Cao, and T. Qian, "Tri-band cross-coupling bandpass filter with rectangular defected ground structure array," *Journal of Electromagnetic Waves and Applications*, Vol. 32, No. 11, 1409–1415, 2018.
5. Ghaderi, A., A. Golestanifar, and F. Shama, "Microstrip bandpass filters using coupled feed lines for third and fourth generation communications," *AEU — International Journal of Electronics and Communications*, Vol. 86, 195–201, 2018.
6. Moitra, S. and R. Dey, "Design of dual band and tri-band Bandpass Filter (BPF) with improved inter-band isolation using DGS integrated coupled microstrip lines structures," *Wireless Personal Communications*, Vol. 110, No. 4, 2019–2030, 2020.
7. Gómez-García, R., L. Yang, J. Muñoz-Ferreras, and D. Psychogiou, "Single/Multi-band coupled-multi-line filtering section and its application to RF diplexers, bandpass/bandstop filters, and filtering couplers," *IEEE Transactions on Microwave Theory and Techniques*, Vol. 67, No. 10, 3959–3972, 2019.

8. Simpson, D. and D. Psychogiou, "Multi-band differential bandpass filters with quasi-elliptic-type passbands and multi-transmission zero common-mode suppression," *IEEE MTT-S International Microwave Symposium*, 1027–1030, 2019.
9. Wu, X.-H., F.-Y. Wan, and J.-X. Ge, "Stub-loaded theory and its application to balanced dual-band bandpass filter design," *IEEE Microwave and Wireless Components Letters*, Vol. 26 No. 4, 231–233, 2016.
10. Du, M. Z., J. X. Chen, and Y. J. Yang, "Balanced dual-band bandpass filter using stub-loaded stepped-impedance resonators," *Journal of Electromagnetic Waves and Applications*, Vol. 27, No. 16, 2056–2064, 2013.
11. Cui, H.-R., Y. Sun, S.-N. Wang, and Y.-L. Lu, "Dual-band differential bandpass filter using stepped impedance resonators," *International Journal of RF and Microwave Computer-Aided Engineering*, Vol. 25, 468–473, 2015.
12. Yang, Z. J., G. X. Xiao, F. Wei, B. Zhou, and B. Li, "A balanced dual-band bandpass filter with independently tunable differential-mode frequencies," *International Journal of RF and Microwave Computer-Aided Engineering*, Vol. 28, e21295, 2018.
13. Cho, Y.-H. and S.-W. Yun, "Design of balanced dual-band bandpass filters using asymmetrical coupled lines," *IEEE Transactions on Microwave Theory and Techniques*, Vol. 61, No. 8, 2814–2820, 2013.
14. Lee, C. H., C. I. G. Hsu, H. H. Chen, and Y.-S. Lin, "Balanced single- and dual-band BPFs using ring resonators," *Progress In Electromagnetics Research*, Vol. 116, 333–346, 2011.
15. Huang, F., J.-P. Wang, J.-S. Hong, and W. Wu, "A new balanced-to-unbalanced filtering power divider with dual controllable passbands and enhanced in-band common-mode suppression," *IEEE Transactions on Microwave Theory and Techniques*, Vol. 67, No. 2, 695–703, 2019.
16. Yang, Y., W.-W. Choi, K.-W. Tam, and L. Zhu, "Balanced dual-band bandpass filter with multiple transmission zeros using doubly short-ended resonator coupled line," *IEEE Transactions on Microwave Theory and Techniques*, Vol.67, No. 7, 1–8, 2015.
17. Ren, B.-P., Z.-W. Ma, H.-W. Liu, X.-H. Guan, X.-L. Wang, P. Wen, and M. Ohira, "Differential dual-band superconducting bandpass filter using multimode square ring loaded resonators with controllable band widths," *IEEE Transactions on Microwave Theory and Techniques*, Vol. 67, No. 2, 726–737, 2019.
18. Wei, F., Y. J. Guo, P. Y. Qin, and X.-W. Shi, "Compact balanced dual- and tri-band bandpass filters based on stub loaded resonators," *IEEE Microwave and Wireless Components Letters*, Vol. 25, No. 2, 76–78, 2015.
19. Zhang, S. X., Z. H. Chen, and Q. X. Chu, "Design of tri-band balanced bandpass filter with controllable frequencies and bandwidths," *IEEE/MTT-S International Microwave Symposium*, Honolulu, Hawaii, USA, 2017.
20. Zhang, S. X., L. L. Qiu, and Q. X. Chu, "Multiband balanced filters with controllable bandwidths based on slotline coupling feed," *IEEE Microwave and Wireless Components Letters*, Vol. 27, No. 11, 974–976, 2017.
21. Ren, B.-P., Z.-W. Ma, H.-W. Liu, X.-H. Guan, P. Wen, C.-Y. Wang, and M. Ohira, "Balanced tri-band bandpass filter using sext-mode stepped-impedance square ring loaded resonators," *IEICE Electronics Express*, Vol. 15, No. 18, 1–6, 2018.
22. Yang, Y., Z.-X. Wang, L. Xu, and Y.-X. Liu, "A balanced tri-band bandpass filter with high selectivity and controllable bandwidths," *International Journal of RF and Microwave Computer-Aided Engineering*, Vol. 29, e21976, 2019.
23. Lee, C. H., C.-I.-G. Hsu, and C. C. Hsu, "Balanced dual-band BPF with stub-loaded SIRs for common-mode suppression," *IEEE Microwave and Wireless Components Letters*, Vol. 20, No. 2, 70–72, 2010.
24. Shen, Y.-J., H. Wang, W. Kang, and W. Wu, "Dual-band SIW differential bandpass filter with improved common-mode suppression," *IEEE Microwave and Wireless Components Letters*, Vol. 25, No. 2, 100–102, 2014.